

# Photocatalytic Degradation of 4-Nitrophenol on Well Characterized Sol–Gel Molybdenum Doped Titania Semiconductors

Rosendo López · Ricardo Gómez

Published online: 19 January 2011  
© Springer Science+Business Media, LLC 2011

**Abstract** Mesoporous  $\text{TiO}_2$ –Mo materials with different Mo contents (0–5.0 wt%) were synthesized by the sol–gel method. In samples annealed at 500 °C, specific surface areas ranging from 150 to 86  $\text{m}^2/\text{g}$  were obtained. X-ray diffraction spectra denoted that the titania anatase phase (~28 nm) was significantly strengthened by the presence of Mo. The UV-vis diffuse reflectance spectra showed that the band gap was shifted to lower energy levels in the samples with higher Mo contents. Fourier transform infrared analysis evidenced that the hydroxylated samples persisted after annealing at 500 °C. X-ray photoelectron spectroscopy analyses showed the presence of  $\text{Mo}^{4+}$  and  $\text{Mo}^{6+}$  species, where  $\text{Mo}^{6+}$  can be transformed from this state to a lower oxidation state during the annealing treatments. The study of the photocatalytic degradation of 4-nitrophenol (4-NP) showed that the activity can be related to the *c* cell parameter of the anatase phase in the Mo-doped semiconductors. Total mineralization of 4-NP up to 98% (TOC) was obtained in the sample (1.0 wt% Mo) with the highest photoactivity.

**Keywords** Sol–gel · Photocatalysts · Photodegradation · Molybdenum oxide · Band-gap energy · 4-Nitrophenol

## 1 Introduction

Titania semiconductors have been confirmed as the most suitable materials for environmental photocatalytic applications. Nowadays, the continuous preparation of improved titania-based photocatalytic materials is the main purpose in research laboratories throughout the world. Transition metals have usually been used as doping agents to obtain photocatalysts with better photoactivity [1–3]. However, metal oxides have been successfully used for the improvement of titania-based photocatalysts. The most common methods that have been reported on titania doping are: Ti-thermal oxidation, plasma spraying, anodization, and chemical vapor deposition [4]. Unfortunately, these techniques require special apparatus and methods that limit the desired properties. On the other hand, soft chemistry catalyst preparation (sol–gel) has been found to be an effective method for the substitution of ions into the  $\text{TiO}_2$  lattice [5]. For example, the incorporation of molybdenum nitrate during the titanium alkoxide gelling step promoted the cationic substitution of  $\text{Ti}^{4+}$  by  $\text{Mo}^{6+}$  in the titania network [6–8]. As for the different publications about metal doping, some authors have claimed that this technique diminishes the band gap energy. In other words, it decreases the energy that is necessary to carry out an electronic transition from the valence band to the conductivity band. In other cases, it has been reported that the dopant creates color centers that induce a red-shift in the absorption spectrum [9], enhancing the absorption by the introduction of additional bands in the solid. Independently of the net effect promoted by the introduction of metal ions into the  $\text{TiO}_2$  lattice, the dopant improves the  $\text{TiO}_2$  photocatalytic activity.

In this study, Mo-doped  $\text{TiO}_2$  photocatalysts were studied. Molybdenum was chosen because its cationic

R. López (✉) · R. Gómez  
Departamento de Química, ECOCATAL, Universidad  
Autónoma Metropolitana-Iztapalapa, Av. San Rafael Atlixco  
No. 186, CP 09340, México DF, México  
e-mail: ross@xanum.uam.mx

R. Gómez  
e-mail: gomr@xanum.uam.mx

radius Mo(VI) ( $0.62 \text{ \AA}$ ) is similar to that of Ti(IV) ( $0.68 \text{ \AA}$ ) and hence the Ti(IV) substitution in the titania network can be possible. The catalysts were prepared by the sol–gel method using as starting precursors ammonium heptamolybdate, and titanium butoxide. The synthesized materials were characterized by nitrogen adsorption, X-ray diffraction, Raman, XPS, UV–vis, and FTIR spectroscopies.

The evaluation of the photocatalytic properties was carried out using 4-nitrophenol (4-NP) as pollutant phenolic organic compound.

## 2 Experimental

### 2.1 Preparation of Photocatalysts

The  $\text{TiO}_2\text{-Mo}$  photocatalysts with different metal concentrations (metal load: 0.1, 0.5, 1.0, and 5.0 wt%) were prepared by the sol–gel method as follows: the corresponding amount of ammonium heptamolybdate tetrahydrate (Sigma-Aldrich) necessary to obtain the desired Mo contents was added to a three neck flask containing 18 mL of deionized distilled water, 44 mL of 1-butanol (Aldrich 99.4%), and 0.2 mL of nitric acid (Aldrich 70% in water to obtain pH 3). Then, 44 mL of titanium (IV) butoxide (Aldrich 97%) were slowly added dropwise to the solution for 4 h (water/alkoxide molar ratio of 8). Afterwards, the solution was heated at  $70^\circ\text{C}$  under reflux and maintained with constant stirring for 24 h until the gel was formed. Finally, the obtained xerogels were dried at  $70^\circ\text{C}$  for 24 h. The dried solids were ground in an agate mortar until fine and homogeneous powder was obtained. Before characterization, all the samples were calcined in air at  $500^\circ\text{C}$  for 4 h using a heating rate of  $2^\circ\text{C}/\text{min}$ . A reference sol–gel  $\text{TiO}_2$  was prepared following the same procedure described above for the  $\text{TiO}_2\text{-Mo}$  samples.

### 2.2 Characterization of Samples

The specific surface area, pore size distribution and pore volume of the solids were determined by the BET method from the nitrogen adsorption isotherms obtained with a Quantachrome Autosorb-3B apparatus. This equipment applies multiple methods of analysis at the same time such as multipoint BET and BJH pore size distribution from the desorption isotherms. Prior to the adsorption, the samples were desorbed under high vacuum at  $200^\circ\text{C}$  for 6 h. The mean pore size diameter distribution was calculated from desorption branch of the isotherm by applying the BJH method.

The X-ray powder diffraction (XRD) patterns were collected at room temperature with a Siemens D-500 diffractometer operated at 40 kV and 30 mA. The  $\text{Cu K}\alpha$

radiation was selected using a graphite monochromator. The measurements were recorded in steps of  $0.03^\circ$  with a count time of 1 s in the  $2\theta$  range from 5 to  $70^\circ$ . The average anatase crystallite size was determined by the Scherrer formula ( $D = K\lambda/\beta \cos \theta$ ), where  $D$  is the crystallite size,  $K$  is a constant equal to 0.94,  $\lambda$  is the wavelength ( $1.5405 \text{ \AA}$ ),  $\theta$  is the diffraction angle, and  $\beta$  is the full width at half maximum (FWHM) of the XRD peak.

The diffuse reflectance spectra (DRS) were obtained with a Varian Cary 100 UV–vis spectrophotometer. The band gap analysis for indirect semiconductors was done through the Kubelka–Munk function ( $F(R)$ ):

$$F(R) = \frac{(1-R)^2}{2R}$$

where  $R$  is the reflectance. The  $E_g$  was calculated from the plot of the modified Kubelka–Munk function,  $[F(R) \times h\nu]^{1/2}$  versus energy of the absorbed light, for indirect semiconductors.

FTIR–ATR spectra were recorded in a Shimadzu IRAffinity-1, in the energy range of  $4000\text{--}350 \text{ cm}^{-1}$ . The samples were mixed with KBr at 5 wt%.

In order to analyze the oxidation state of the doping metal in the titania semiconductors, X-ray photoelectron spectroscopy (XPS) was used. The electron spectrometer was a Thermo VG Scientific ESCALAB 250 equipped with hemispherical analyzer equipment. The operating conditions of the spectrometer were set at constant pass energy mode and monochromatized  $\text{AlK}\alpha$  radiation ( $h\nu = 1486.6 \text{ eV}$ ) was used. The X-ray source operated at 10 mA and 15 kV. The intensities of the peaks were estimated by calculating the integral of each peak after subtracting the S-shaped background and fitting the experimental peak with a combination of Lorentzian/Gaussian lines of variable proportions. The binding energies (BE) were referenced to the C (1 s) peak, which was fixed at 284.6 eV.

The samples were also characterized by Fourier-transform Raman spectroscopy using a Thermo Nicolet Almega dispersive Raman system with a wavelength emission of 532 nm using an Nd:YVO<sub>4</sub> laser source and a nominal power of 25 mW. Spectra resolution gratings were used to give a spectral resolution of  $2 \text{ cm}^{-1}$ . The spectra were recorded at room temperature from 4250 to  $100 \text{ cm}^{-1}$  with an exposure time of 1 s and 16 repetitions.

### 2.3 Photocatalytic Degradation

The activity of the samples was evaluated in the 4-nitrophenol (4-NP) degradation. The photocatalytic reaction was carried out in a glass reactor containing 200 ml of the aqueous solution at 30 ppm of the organic molecule and 0.2 g of photocatalyst. The powder suspension was stirred

and irradiated with a high pressure mercury lamp (UV lamp, emitting at 254 nm, 2.16 w, 18 mA) protected with a quartz tube and immersed in the solution. To assure the adsorption–desorption equilibrium of the molecule in the solution, the suspension was stirred for 30 min in the dark with an air flow of 2 ml/s (Air-Pump BOYU S-4000B) and then irradiated with the UV lamp (Pen-Ray UVP). The degradation of the pollutant was monitored by taking a sample every 20 min and following the main section of the 4-NP absorption band at 316 nm using a UV-vis spectrophotometer Varian Cary 100 UV-vis. Each sample was filtered through a nylon membrane (0.45 µm, Millipore) to remove the oxide particles before analysis.

To determine the reached mineralization, total organic carbon (TOC) measurements were carried out with a Shimadzu TOC-V CPN (equipped with a NDIR detector).

### 3 Results and Discussion

#### 3.1 Characterization

##### 3.1.1 Nitrogen Adsorption

Figure 1 shows the selected adsorption–desorption isotherms for the  $\text{TiO}_2$ –Mo samples (0.5, 1.0, and 5.0 wt%) annealed at 500 °C. All the samples exhibited the type IV nitrogen isotherm, which is characteristic of mesoporous materials [10]. For Mo contents below 5%, a clear H1 type hysteresis loop at relative pressures between 0.67 and 0.87 related to capillary condensation [11] can be observed. This is characteristic of solids consisting of particles (crossed by nearly cylindrical channels), aggregates or agglomerates of spheroidal particles with pores of uniform size and shape.

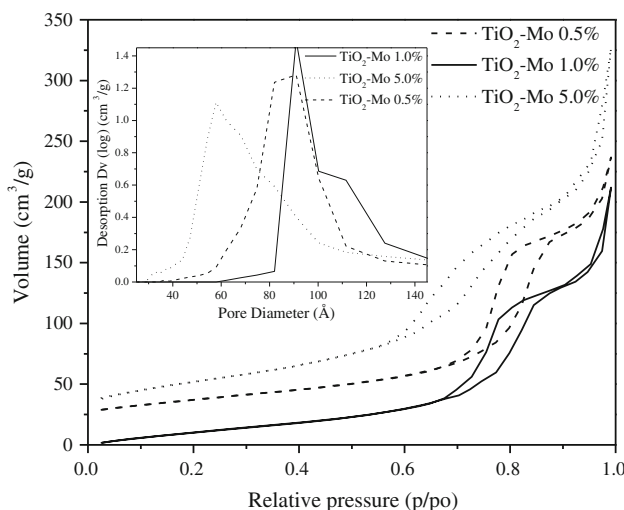


**Fig. 1** Nitrogen adsorption–desorption isotherms for the  $\text{TiO}_2$ –Mo solids at 0.5, 1.0, and 5.0 wt%, insert pore size distribution

The monomodal pore size distribution (Fig. 1) derived from the desorption branches of the isotherms indicate relatively regular mesoporous channels of Ca. 9.0 nm. However, when the Mo content is 5 wt%, the mesoporosity is decreased (5.8 nm) because of the presence of Mo oxide conglomerates blocking the pore access of the solid [12]. The BET specific surface areas of the doped samples are higher than that of pure titania (Table 1). Nevertheless, there is no significant effect due to the metal loading regarding pure  $\text{TiO}_2$ .

#### 3.1.2 Powder X-ray Diffraction

The crystalline structure of the  $\text{TiO}_2$ –Mo mesoporous materials are shown in Fig. 2. The diffraction patterns of the undoped and doped materials annealed at 500 °C only exhibit peaks at  $2\theta$  angles of 25.38 (101), 38.14 (004), 48.04 (200), and 53.89 (105), which correspond to the anatase phase (JCPDS 21-1272). This result indicates that the structure is preserved by the incorporation of Mo to the lattice. The presence of any molybdenum oxide (as  $\text{MoO}_3$ ) was not detected for any of the different doping contents, and probably, only a molybdenum titanate signal is overlapped with the main reflections associated to the plane (101) and (200) of anatase. As the radius of the Mo (VI) ion (0.62 Å) gets closer to that of Ti(IV) (0.68 Å), the Mo (VI) ions can either interstitially substitute Ti(IV) into the  $\text{TiO}_2$  lattice or act as a substitutional impurity. The (101) and (200) peaks of the anatase crystal planes were selected to determine the lattice parameters of the doped photocatalysts (Table 2). According to Vegard's law, the lattice constant of a solid is increased with the increase in the solute concentration, which occurs when the radius of the

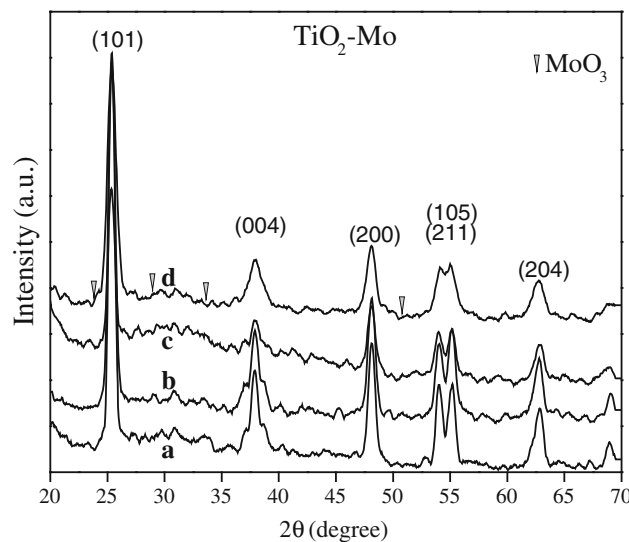


**Fig. 2** X-ray diffraction patterns for the  $\text{TiO}_2$ –Mo solids, **a** 0.1 wt%. **b** 0.5 wt%. **c** 1.0 wt%. **d** 5.0 wt%

**Table 1** Specific surface area, pore volume, and mean pore size for the TiO<sub>2</sub>–Mo photocatalysts

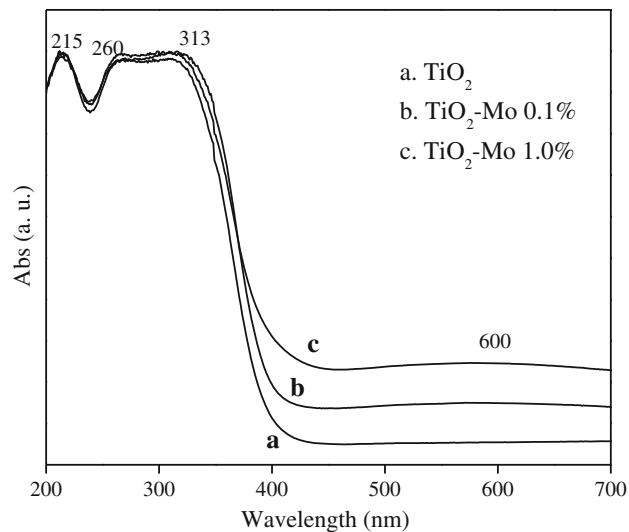
| Doping (wt%)     | Surface area (m <sup>2</sup> /g) | Pore volume (cm <sup>3</sup> /g) | Pore size (nm) |
|------------------|----------------------------------|----------------------------------|----------------|
| 0.1              | 96                               | 0.35                             | 9.1            |
| 0.5              | 94                               | 0.35                             | 8.1            |
| 1.0              | 86                               | 0.27                             | 8.8            |
| 5.0              | 155                              | 0.50                             | 5.8            |
| TiO <sub>2</sub> | 70                               | 0.27                             | 12.1           |

solute atom is larger than that of the solvent atom. The opposite effect occurs when the radius of the solute atom is smaller than that of the solvent atom [13]. The charge on Mo (VI) exceeds that of Ti(IV), thus charge compensation is achieved by decreasing the oxygen vacancies, which stabilizes the crystalline phase. The variation in the lattice parameters could indicate the modification of oxygen vacancies that are usually created with the incorporation of an impurity [14].

The crystallite size obtained by Scherrer equation shows that the solids are nanostructured. The crystallite size decreases with the Mo content, except for the 5.0 wt% samples. In this solid, the presence of Mo<sup>4+</sup> (not detected by XRD, but observed by XPS) produced a diminution in the crystallite size (Table 2).

### 3.1.3 UV–Vis Adsorption and Diffuse Reflectance Spectroscopy

To observe the optical response of TiO<sub>2</sub>–Mo as a function of the doping content, the UV–visible absorption spectra were recorded in a wavelength between 200 and 800 nm, Fig. 3. The effect of incorporating Mo into the TiO<sub>2</sub> lattice is evident by comparing the undoped material with the doped one. A significant difference between the bare TiO<sub>2</sub> and the low doped material (0.1 wt%) cannot be observed. However, the

**Fig. 3** UV–vis spectra for the TiO<sub>2</sub>–Mo materials, **a** TiO<sub>2</sub>, **b** 0.1 wt%. **c** 1.0 wt%

increase of the absorbance in the doped material can be noted. In all the TiO<sub>2</sub>–Mo samples, a broad band approximately centered at 600 nm can be ascribed to a Mo<sup>5+</sup>–Mo<sup>6+</sup> charge transfer or a Mo<sup>5+</sup> d-d transition [15]. A strong absorption band between 300 and 400 nm arises from O<sub>2p</sub>→Ti<sub>3d</sub> transitions in tetrahedral symmetry, which is modified by the slight incorporation of Mo [16, 17]. The presence of two shoulders around 200–235 and 260–330 nm, for all the doped and undoped materials, corresponds to the A<sub>1</sub> and A<sub>2</sub> bands associated with bulk crystals and represent the electronic transitions from  $\Gamma_{15}\rightarrow\Gamma_{12}$  and  $\Gamma_{25}\rightarrow\Gamma_{12}$ , respectively. The split of A<sub>2</sub>–A<sub>1</sub> can be associated with the presence of Mo<sup>6+</sup> in the TiO<sub>2</sub> structure [18–20].

The band gap energy (Eg) was calculated from the modified Kubelka–Munk plot (Fig. 4). The Eg values were obtained considering indirect transitions of the TiO<sub>2</sub>–Mo semiconductors. As it can be seen in Table 2 the Eg values for the solids with 0.1, 0.5, and 1.0 wt% Mo decrease from

**Table 2** Structural parameters for the TiO<sub>2</sub>–Mo-doped materials

| Photocatalyst (wt%)       | 2θ               | d <sub>hkl</sub> | Unit cell volume (Å) <sup>3</sup> | Lattice parameters (Å)   | Crystallite size (nm) | Eg (eV) |
|---------------------------|------------------|------------------|-----------------------------------|--------------------------|-----------------------|---------|
| TiO <sub>2</sub> S-G      | 25.436<br>48.116 | 3.498<br>1.889   | 132.244                           | a = b = 3.779, c = 9.259 | 40.5                  | 3.20    |
| TiO <sub>2</sub> –Mo 0.1% | 25.370<br>48.175 | 3.507<br>1.887   | 135.313                           | a = b = 3.774, c = 9.496 | 37.45                 | 3.15    |
| TiO <sub>2</sub> –Mo 0.5% | 25.338<br>48.127 | 3.512<br>1.889   | 136.021                           | a = b = 3.778, c = 9.528 | 28.68                 | 3.12    |
| TiO <sub>2</sub> –Mo 1.0% | 25.290<br>48.111 | 3.518<br>1.889   | 137.708                           | a = b = 3.779, c = 9.640 | 27.72                 | 3.10    |
| TiO <sub>2</sub> –Mo 5.0% | 25.354<br>48.079 | 3.510<br>1.890   | 134.862                           | a = b = 3.781, c = 9.429 | 19.95                 | 3.18    |

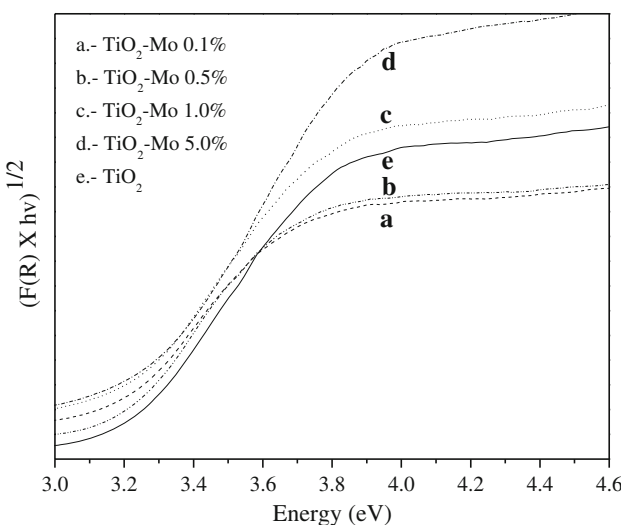


**Fig. 4** Kubelka–Munk modified spectra for the  $\text{TiO}_2$ –Mo semiconductors, **a** 0.1 wt%. **b** 0.5 wt%. **c** 1.0 wt%. **d** 5.0 wt%. **e**  $\text{TiO}_2$

3.15 to 3.10 eV as a consequence of the increase in the molybdenum percentage. However, the highest value (3.18 eV) corresponds to the sample with the highest Mo content. When the  $\text{Mo}^{6+}$  ion amount is too high, the  $\text{TiO}_2$  is covered with the Mo in excess (the material color is a signal of the molybdenum excess) and it can promote the absorption of light at relatively high energies. On the other hand, it is important to note that all the  $E_g$  values are lower than the value obtained for the bare  $\text{TiO}_2$  (3.20 eV).

#### 3.1.4 Fourier Transform Infrared spectroscopy

FTIR spectra of  $\text{TiO}_2$ –Mo under KBr were taken in order to analyze the structure of the materials (Fig. 5). At the

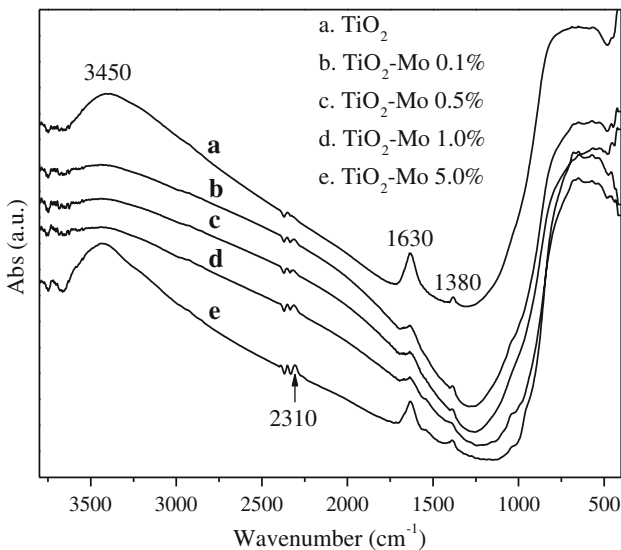


**Fig. 5** FTIR spectra for the  $\text{TiO}_2$ –Mo solids annealed at 500 °C, **a**  $\text{TiO}_2$  wt%. **b** 0.1 wt%. **c** 0.5 wt%. **d** 1.0 wt%. **e** 5.0 wt%

3450  $\text{cm}^{-1}$  region, the OH vibration bands can be observed. At 1630  $\text{cm}^{-1}$ , the vibration frequency due to the OH bending vibration band of water in the gel can be seen. Both vibration bands (1630 and 3450  $\text{cm}^{-1}$ ) can be attributed to the surface of adsorbed water molecules and surface adsorbed hydroxyl groups [7, 21, 22]. The absorption band observed at 2310  $\text{cm}^{-1}$  can be assigned to the Mo–O vibrations [8]. Finally, in the low-energy region (420–690  $\text{cm}^{-1}$ ) low intensity bands related to the stretching vibration of the Ti–O and Ti–O–Ti bonds, typical of titanium dioxide, can be seen.

#### 3.1.5 X-ray Photoelectron Spectroscopy

To identify the oxidation state of molybdenum in the nanostructured  $\text{TiO}_2$ –Mo photocatalysts, the XPS analysis was carried out. For practical purposes, only the 1.0 wt% Mo sample was analyzed. The deconvolution for the Mo (3d) core level binding energy (BE) in the selected sample is presented in Fig. 6. All the peaks were calibrated at the C 1 s peak (284.5 eV), which corresponds to carbon and is always present on the surface of the powdered samples (adventitious carbon). The characteristic peaks for the Ti 2p (not showed) situated at the binding energies (BE) between 554 and 564 eV was present in all samples. In the deconvoluted signals assigned to Mo (3d) appear two maximums that correspond to the 3d 5/2 core level binding energy. The first, at 230 eV is associated with  $\text{Mo}^{4+}$  and the second one, at 231.9 eV, corresponds to  $\text{Mo}^{6+}$  [23, 24]. The energy difference between the 3d<sub>5/2</sub> and 3d<sub>3/2</sub> (3.2 eV) corresponds to  $\text{MoO}_3$  oxide and it must be constant for any

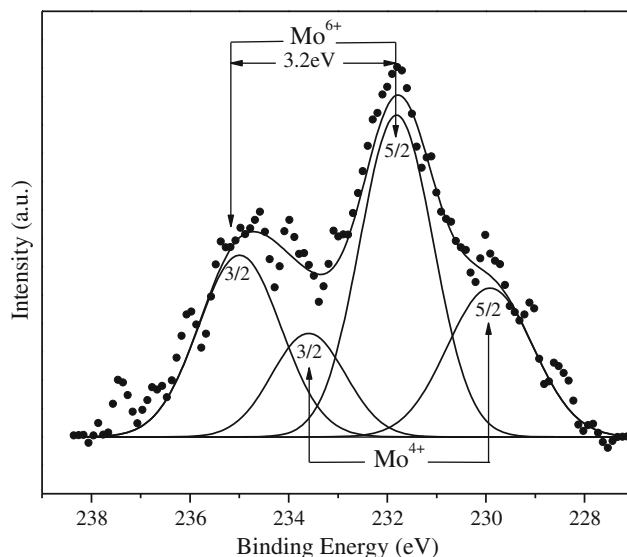


**Fig. 6** X-ray photoelectron spectra for the  $\text{TiO}_2$ –Mo semiconductors for Mo (3d) core level binding energy

doping content [23]. The analysis of the integral area under these curves reveals that  $\text{Mo}^{6+}$  is the predominant species (64.7%) while the  $\text{Mo}^{4+}$  relative percentage is 35.3%. It is important to note that the  $\text{Mo}^{6+}$  cationic oxidation state of the precursor appears as  $\text{Mo}^{4+}$  in the annealed sample. The reduction of cationic species in the sol–gel preparations was also observed for  $\text{Ti}^{4+}$ ,  $\text{Pt}^{4+}$ , and  $\text{Pd}^{2+}$  and it is explained as the result of the strong reductive character of the hydroxyl groups formed during the dehydroxylation step [25–28]. For the O 1 s region, the main signal is located at 528.77 eV and it corresponds to Ti–O bonds in the  $\text{TiO}_2$  lattice and Ti–OH hydroxyl groups. The presence of Ti–OH arises from the synthesis method. The physically adsorbed  $\text{H}_2\text{O}$  can react with  $\text{TiO}_2$  to form Ti–OH [29].

### 3.1.6 Raman Spectroscopy

Raman spectroscopy was used in order to elucidate the structural modification of the  $\text{TiO}_2$  as a function of molybdenum content. The Raman spectra are shown in Fig. 7. All the samples exhibit approximately same bands located at 145 ( $B_{1g}$ ), 323 ( $B_{1g} + A_{1g}$ ), 399 ( $B_{1g}$ ), 521 ( $E_g$ ), and 642 ( $E_g$ )  $\text{cm}^{-1}$ , which correspond to the crystalline anatase phase. An additional band (very weak) located at 798  $\text{cm}^{-1}$  can be assigned to the first overtone of the 399  $\text{cm}^{-1}$  band of the  $\text{TiO}_2$  anatase phase [30, 31]. The effect related to the molybdenum content on the crystallinity and crystallite size can be evaluated from the intensity and width of the Raman signals. As the molybdenum content increases, the intensity of all the bands diminishes. The peak located at 145  $\text{cm}^{-1}$  practically disappears when the molybdenum content is 5 wt%. Is important to note that the signal located near at 399  $\text{cm}^{-1}$  is displaced at low

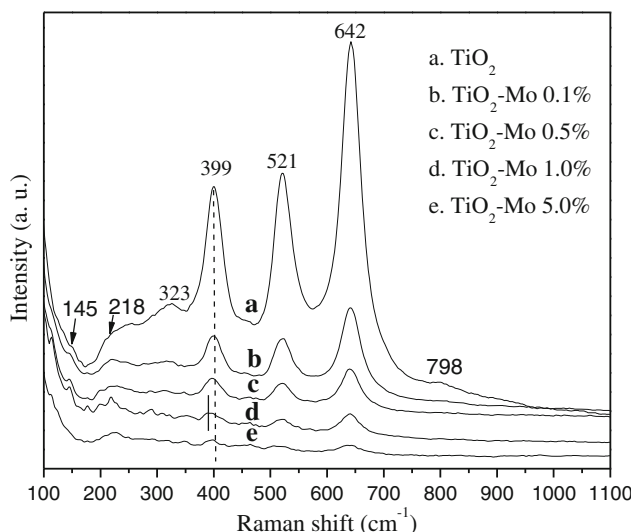


**Fig. 7** Raman spectra for the  $\text{TiO}_2$ -Mo solids, **a**  $\text{TiO}_2$  wt%. **b** 0.1 wt%. **c** 0.5 wt%. **d** 1.0 wt%. **e** 5.0 wt%

frequency, around 9  $\text{cm}^{-1}$ , in the doping content of 1.0 wt%, this indicate a perturbation in the Ti–O–Ti structure by the Mo ions. The signals due to the presence of molybdenum oxide are not present in the spectra (960–990  $\text{cm}^{-1}$ ), which suggests either the substitution of  $\text{Ti}^{4+}$  by  $\text{Mo}^{6+}$  in the titania network or the formation of well dispersed molybdenum oxide on the titania surface, which is not detectable neither by Raman spectroscopy nor XRD analysis.

### 3.1.7 Photocatalysis

In this article, photocatalyst powder was used in suspended solutions because of the advantage associated with a higher reactive surface that is not found in fixed thin films. The purpose of using a UV lamp emitting at 254 nm was to provide, at least, the minimum energy required for the activation of the semiconductor. The  $\text{TiO}_2$ -Mo samples were mixed with 200 mL of the solution containing 4-nitrophenol and stirred in the dark to ensure the complete adsorption between the solid powder and the organic molecule and the photocatalytic reaction was followed for 210 min. The photoactivity as a function of time for all the doped samples and P-25 (Degussa, as reference) is shown in Fig. 8. The photodegradation follows a pseudo-first order reaction and it is represented in Fig. 9. The constant rate as well as the half-life,  $t_{1/2}$  (min or s), can be calculated from Fig. 8 by using a first order equation:

$$t_{1/2} = \frac{\ln 2}{k}$$

where k is the rate constant, the results are reported in Table 3. The  $t_{1/2}$  increased values are found between 38 and 79 min. The lowest value corresponds to the samples

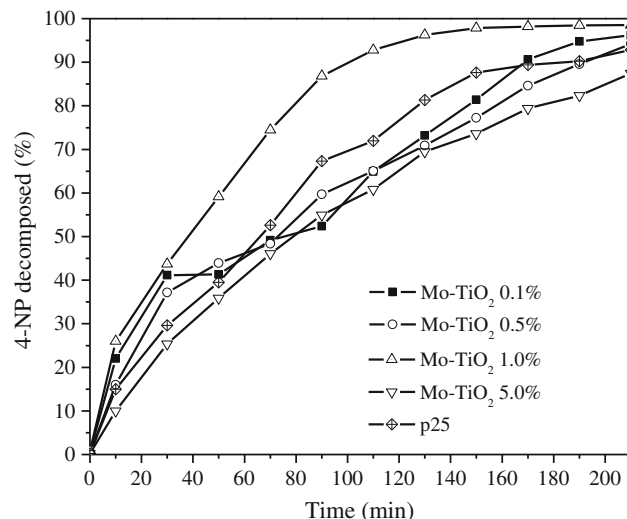


**Fig. 8** Photocatalytic activity for the 4-nitrophenol decomposition as function of time

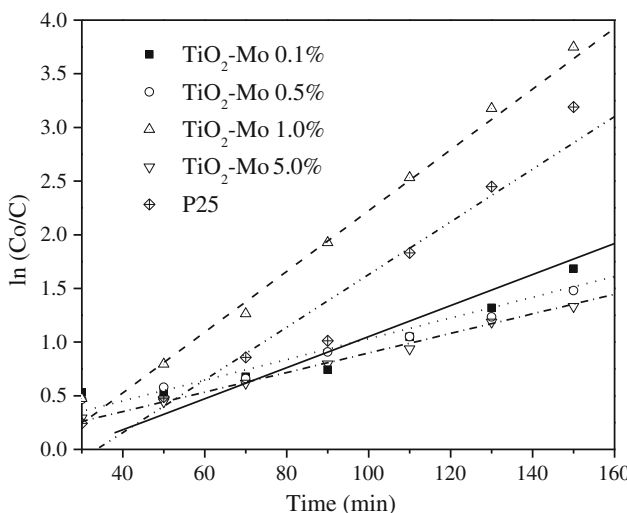


**Fig. 9** First order kinetics for the 4-nitrophenol photodegradation on the Mo-doped  $\text{TiO}_2$  semiconductors

**Table 3** Kinetic values for the 4-nitrophenol photodecomposition and total organic carbon TOC for the  $\text{TiO}_2\text{-Mo}$  semiconductors

| Doping (wt%) | $k^a$ ( $\text{min}^{-1}$ ) | $t_{1/2}$ (min) | Decomposed 4-NP (%) | TOC <sup>b</sup> (mg/L) | TOC <sup>c</sup> (%) |
|--------------|-----------------------------|-----------------|---------------------|-------------------------|----------------------|
| 0.1          | 9.24                        | 75              | 96                  | 6                       | 94                   |
| 0.5          | 9.49                        | 72              | 94                  | 12                      | 88                   |
| 1.0          | 18.24                       | 38              | 98                  | 5                       | 95                   |
| 5.0          | 8.77                        | 79              | 87                  | 33                      | 67                   |
| P25          | 10.50                       | 66              | 92                  | 14                      | 86                   |

<sup>a</sup> Rate constant ( $\times 10^{-3}$ )

<sup>b</sup> Residual TOC 4-NP

<sup>c</sup> Removed 4-NP

with 1 wt% Mo, and the highest one to the sample with 5 wt% Mo. It must be noted that the highest activity is presented by the catalyst with 1.0 wt% Mo, which is the semiconductor with the lowest band gap energy (3.10 eV), Table 2. The interest in preparing doped semiconductors by the sol–gel method was to allow the incorporation of the doping cation into the titania network under soft chemistry conditions. The extent of the  $\text{Ti}^{4+}$  substitution by  $\text{Mo}^{6+}$  cations can be estimated from the  $c$  cell parameter and from the unit cell volume values. If it is assumed that a large cell parameter denotes an important strength of the crystallite unit cell i.e. a high perturbation of the  $\text{Ti}-\text{O}-\text{Ti}$  bonds by the formation of  $\text{Ti}-\text{O}-\text{Mo}$  bonds, it can be said that in the sample with 1.0 wt% Mo, the highest  $\text{Ti}^{4+}$  substitution was reached. In order to support this assumption, Fig. 10, represents the photodegradation of the 4-NP as a function of molybdenum content and compares it with the  $c$  cell parameter values. The good agreement between the  $\text{Ti}^{4+}$  substitution extent (determined by the cell parameter

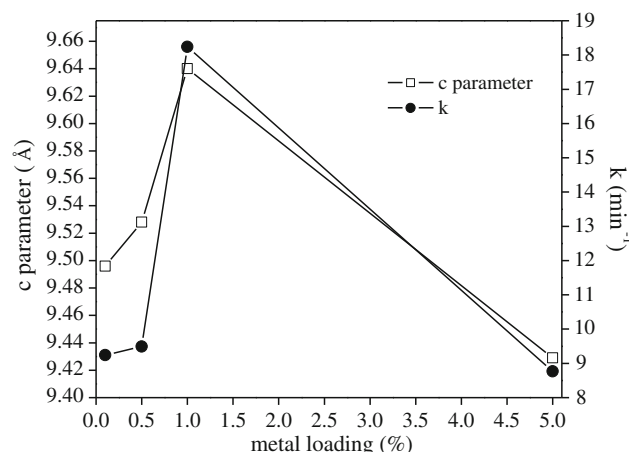


**Fig. 10** Photocatalytic degradation of 4-nitrophenol and  $c$  anatase cell parameter as function of Mo content for the  $\text{TiO}_2\text{-Mo}$  photocatalysts

enlargement) and the photocatalytic activity is also shown in Fig. 10.

The determination of the total decomposition of organic compounds can be evaluated by measuring the total organic carbon (TOC) in the irradiated solution. In the present study, aliquots of the solution containing 4-NP were analyzed after 210 min under irradiation and the corresponding results are reported in Table 3. TOC values up to 95% were obtained. These values show that the  $\text{TiO}_2\text{-Mo}$  catalysts synthesized in this study are very efficient for the total oxidation of 4-NP. The possible presence of the chlorocatechol (4-CC) and hydroquinone (HQ) intermediaries, which have been reported elsewhere for the 4-NP decomposition [32–35], are not evaluated in the present study due to the high mineralization achieved in the photooxidation process.

#### 4 Conclusions

The doping of titanium alkoxide with Mo allows the formation of highly hydroxylated solids with high specific surface area and well defined anatase nanocrystalline phase. An important modification of the anatase  $c$  cell parameter was observed by the presence of Mo at 1.0 wt%. A slight shift to the low energy region of the band gap energy was produced in the Mo-doped samples. It has been shown that the photocatalytic activity for the 4-nitrophenol degradation on Mo-doped samples is a function of the anatase  $c$  cell parameter.

**Acknowledgments** R. López acknowledges the scholarship by CONACYT México. R. Gómez acknowledges the CONACYT CB-2006-1-62053 grant: preparation of semiconductors by the sol–gel method.

## References

1. Di Paola A, Garcia López E, Marci G, Martin C, Palmisano L, Rives V, Venezia AM (2004) *Appl Catal B Environ* 48:223
2. Litter MI (1999) *Appl Catal B Environ* 23:89
3. Dvoranová D, Brezová V, Mazúr M, Malati MA (2002) *Appl Catal B Environ* 37:91
4. Fujishima A, Honda K (1972) *Nature* 238:37
5. Lopez T, Rojas F, Alexander-Katz R, Galindo F, Balakin A, Buljan A (2004) *J Solid State Chem* 177:1873
6. Du Y, Gan Y, Yang P, Cuie Z, Hua N (2007) *Mater Chem Phys* 103:446
7. Gomathi Devi L, Girish Kumar S, Narasimha Murthy B, Kottam Nagaraju (2009) *Catal Commun* 10:794
8. Gomathi Devi L, Narasimha Murthy B (2008) *Catal Lett* 125:320
9. Serpone N (2006) *J Phys Chem B* 110:24287
10. IUPAC (1985) *Pure Appl Chem* 57:603
11. Burgess CGV, Everett DH, Nuttall S (1989) *Pure Appl Chem* 61:1845
12. López T, Gómez R (1994) In: Klein LC (ed) *Sol-Gel optics: processing and applications*, chap. 16. Kluwer Academic Publishers, MA, p 345
13. Azaroff LV (1997) *Introduction to solids*. McGraw Hill Inc, NY
14. Prasad K, Bally P, Schmid E, Lévy F, Benoit J, Barthou C, Be-nalloul P (1997) *J Appl Phys* 36:5696
15. Dieterle M, Weinberg G, Mesta G (2002) *Phys Chem Chem Phys* 4:812
16. Sanjinés R, Tang H, Berger H, Gozzo F, Margaritondo G, Lévy F (1994) *J Appl Phys* 75:2945
17. Chen J, Lin LB, Jing FQ (2001) *J Phys Chem Solids* 62:1257
18. Kutty TRN, Gomathi Devi L (1985) *Mater Res Bull* 20:793
19. Fuller MP, Griffiths PR (1978) *Anal Chem* 5013:1906
20. Cardona M, Harbeke G (1964) *Phys Rev* 137A:1467
21. Lopez T, Sanchez E, Bosch P, Meas Y, Gomez R (1992) *Mater Chem Phys* 32:141
22. Van Thiel M, Becker ED, Pimentel GC (1957) *J Chem Phys* 27:486
23. Wagner CD, Riggs WM, Davis LE, Moulder JF, Mullenberg GE (1979) *Handbook of x-ray photoelectron spectroscopy*. Physical Electronic Division, Perkin-Elmer Corporation
24. Li YX, Galatsis K, Wlodarski W, Passacantando M, Santucci S, Siciliano P, Catalano M (2001) *Sens Actuators B* 77:27
25. Muñoz E, Boldú JL, Andrade E, Novaro O, Bokhimi X, López T, Gómez R (2001) *J Am Ceram Soc* 84:392
26. Gómez R, López T, Bokhimi X, Muñoz E, Boldú JL, Novaro O (1998) *J Sol-Gel Sci Technol* 11:309
27. Boldú JL, Muñoz E, Bokhimi X, Novaro O, López T, Gómez R (1999) *Langmuir* 15:32
28. Lopez T, Tzompantzi F, Navarrete J, Gomez R, Boldú JL, Muñoz E, Novaro O (1999) *J Catal* 181:285
29. Yu JC, Yu J, Zhao J (2002) *Appl Catal B Environ* 36:31
30. Alemany L, Lietti L, Ferlazzo N, Forzatti P, Busca G, Giannello E, Bregani F (1995) *J Catal* 155:117
31. Ocana M, Garcia Ramos JV, Serna CJ (1992) *J Am Ceram Soc* 75:2010
32. Stafford U, Gray KA, Kammat PV (1997) *J Catal* 167:25
33. Al-Ekabi H, Serpone N (1988) *J Phys Chem* 92:5726
34. Mills A, Morris S, Davies RJ (1993) *Photochem Photobiol A Chem* 70:183
35. Mills A, Morris SJ (1993) *J Photochem Photobiol A Chem* 71:75